SARS-CoV-2 spike P681R mutation enhances and accelerates viral fusion

Akatsuki Saito[1,2,3,16], Hesham Nasser[4,5,16], Keiya Uriu[6,16], Yusuke Kosugi[6,16], Takashi Irie[7,16], Kotaro Shirakawa[8], Kenji Sadamasu[9], Izumi Kimura[6], Jumpei Ito[6], Jiaqi Wu[10,11], Seiya Ozono[12], Kenzo Tokunaga[12], Erika P Butlertanaka[1], Yuri L Tanaka[1], Ryo Shimizu[4,13], Kenta Shimizu[14], Takasuke Fukuhara[14], Ryoko Kawabata[7], Takemasa Sakaguchi[7], Isao Yoshida[9], Hiroyuki Asakura[9], Mami Nagashima[9], Kazuhisa Yoshimura[9], Yasuhiro Kazuma[8], Ryosuke Nomura[8], Yoshihito Horisawa[8], Akifumi Takaori-Kondo[8], The Genotype to Phenotype Japan (G2P-Japan) Consortium, So Nakagawa[10,11]*, Terumasa Ikeda[4]*, Kei Sato[6,11,15,17]*.

[1] Department of Veterinary Science, Faculty of Agriculture, University of Miyazaki, Miyazaki 8892192, Japan
[2] Center for Animal Disease Control, University of Miyazaki, Miyazaki 8892192, Japan
[3] Graduate School of Medicine and Veterinary Medicine, University of Miyazaki, Miyazaki 8892192, Japan
[4] Division of Molecular Virology and Genetics, Joint Research Center for Human Retrovirus infection, Kumamoto University, Kumamoto 8600811, Japan
[5] Department of Clinical Pathology, Faculty of Medicine, Suez Canal University, Ismailia 41511, Egypt
[6] Division of Systems Virology, Department of Infectious Disease Control, International Research Center for Infectious Diseases, The Institute of Medical Science, The University of Tokyo, Tokyo 1088639, Japan
[7] Institute of Biomedical and Health Sciences, Hiroshima University, Hiroshima 7348551, Japan
[8] Department of Hematology and Oncology, Graduate School of Medicine, Kyoto University, Kyoto 6068507, Japan
[9] Tokyo Metropolitan Institute of Public Health, Tokyo 1690073, Japan
[10] Department of Molecular Life Science, Tokai University School of Medicine, Kanagawa 2591193, Japan
[11] CREST, Japan Science and Technology Agency, Saitama 3220012, Japan
[12] Department of Pathology, National Institute of Infectious Diseases, Tokyo 1628640, Japan
[13] Graduate School of Medical Sciences, Kumamoto University, Kumamoto 8600811, Japan
[14] Department of Microbiology and Immunology, Graduate School of Medicine, Hokkaido University, Hokkaido 0608638, Japan
[15] Twitter: @SystemsVirology
[16] These authors contributed equally

[17] Lead Contact
*Correspondences:
so@tokai.ac.jp (S.N.)
ikedat@kumamoto-u.ac.jp (T.Ikeda)
KeiSato@g.ecc.u-tokyo.ac.jp (K.Sato)

Conflict of interest: The authors declare that no competing interests exist.
Short title: A SARS-CoV-2 spike mutation promotes viral fusion (49/50 characters)
Keywords: SARS-CoV-2; COVID-19; spike protein; B.1.617; P681R; fusion

Highlights (85 characters including spaces)

- P681R mutation is highly conserved in the B.1.617 lineages
- P681R mutation accelerates and enhances SARS-CoV-2 S-mediated fusion
- Promotion of viral fusion by P681R mutation is augmented by TMPRSS2

Summary (150/150 words)
During the current SARS-CoV-2 pandemic, a variety of mutations have been accumulated in the viral genome, and at least five variants of concerns (VOCs) have been considered as the hazardous SARS-CoV-2 variants to the human society. The newly emerging VOC, the B.1.617.2 lineage (delta variant), closely associates with a huge COVID-19 surge in India in Spring 2021. However, its virological property remains unclear. Here, we show that the B.1.617 variants are highly fusogenic and form prominent syncytia. Bioinformatic analyses reveal that the P681R mutation in the spike protein is highly conserved in this lineage. Although the P681R mutation decreases viral infectivity, this mutation confers the neutralizing antibody resistance. Notably, we demonstrate that the P681R mutation facilitates the furin-mediated spike cleavage and enhances and accelerates cell-cell fusion. Our data suggest that the P681R mutation is a hallmark characterizing the virological phenotype of this newest VOC, which may associate with viral pathogenicity.

Introduction

In December 2019, an unusual infectious disease, now called coronavirus disease 2019 (COVID-19), emerged in Wuhan, Hubei province, China (Wu et al., 2020; Zhou et al., 2020). Severe acute respiratory syndrome coronavirus 2 (SARS-CoV-2), the causative agent of COVID-19, has rapidly spread all over the world, and as of June 2021, SARS-CoV-2 is an ongoing pandemic: more than 170 million cases of infections have been reported worldwide, and more than 3.5 million people died of COVID-19 (WHO, 2021a).

During the current pandemic, SARS-CoV-2 has acquired a variety of mutations [reviewed in (Plante et al., 2021)]. First, in the spring of 2020, a SARS-CoV-2 derivative harboring the D614G mutation in its spike (S) protein has emerged and quickly become predominant (Korber et al., 2020). Because the D614G mutation increases viral infectivity, fitness, and inter-individual transmissibility (Hou et al., 2020; Ozono et al., 2021; Plante et al., 2020; Volz et al., 2021; Yurkovetskiy et al., 2020; Zhou et al., 2021), the D614G-bearing variant has quickly swept out the original strain. Since the fall of 2020, some SARS-CoV-2 variants bearing multiple mutations have emerged and rapidly spread worldwide. As of June 2021, there have been at least five variants of concern (VOC): B.1.1.7 (alpha variant), B.1.351 (beta variant), P.1 (gamma variant), B.1.427/429 (epsilon variant; note that this variant has been downgraded to a variant of interest in May 2021) and B.1.617.2 (delta variant), and these lineages respectively emerged in the UK, South Africa, Brazil, the USA and India (CDC, 2021; WHO, 2021b).

As a common characteristic of VOCs, these variants tend to be relatively resistant to the neutralizing antibodies (NAbs) that were elicited in convalescent and vaccinated individuals [reviewed in (Corti et al., 2021; Harvey et al., 2021)]. In fact, recent investigations have revealed that B.1.1.7 (Chen et al., 2021; Collier et al., 2021; Wang et al., 2021b), B.1.351 (Chen et al., 2021; Garcia-Beltran et al., 2021; Hoffmann et al., 2021; Liu et al., 2021b; Planas et al., 2021; Wang et al., 2021b), P.1 (Garcia-Beltran et al., 2021; Hoffmann et al., 2021; Wang et al., 2021a) and B.1.427/429 (Deng et al., 2021) are differentially resistant to the NAbs derived from COVID-19 convalescents and vaccinees. Because the receptor binding domain (RBD) of SARS-CoV-2 S protein is immunodominant, approximately 90% of the NAbs present in anti-SARS-CoV-2 sera targets this domain (Piccoli et al., 2020). On the other hand, some SARS-CoV-2 variants including VOCs have acquired mutation in the RBD, such as the E484K mutation (Garcia-Beltran et al., 2021; Hoffmann et al., 2021), to evade antiviral immunity.

At the end of 2020, the B.1.617 lineage has emerged in India, and this variant is thought to be a main driver of a massive COVID-19 surge in India, which

107 has peaked 400,000 infection cases per day (Singh et al., 2021). The B.1.617
108 lineage includes three sublineages, B.1.617.1, B.1.617.2 and B.1.617.3, and a
109 sublineage, B.1.617.2, is the latest VOC (CDC, 2021; WHO, 2021b). Importantly,
110 early evidence from the Public Health England has suggested that the B.1.617.2
111 may have an increased risk of hospitalization compared to the B.1.1.7 cases (PHE,
112 2021).
113 Compared to the other VOCs, there are at least two common features in
114 the S protein of the B.1.617 lineage. One is the L452R mutation, which is shared
115 with the B.1.427/429 lineage. Because recent studies including ours have shown
116 that the L452R mutation increases viral infectivity and fusogenicity (Deng et al.,
117 2021; Motozono et al., 2021), the L452R mutation in the B.1.617 variant can
118 contribute to the accelerated spread of this variant in the human population. The
119 other is the substitution at the position 484 of S protein; the B.1.617.1 and B.1.617.3
120 variants possess the E484Q mutation, while the two VOCs, B.1.351 and P.1,
121 possess E484K (CDC, 2021; WHO, 2021b).Intriguingly, both the E484K (Baum et
122 al., 2020; Chen et al., 2021; Liu et al., 2021c; Wang et al., 2021b; Weisblum et al.,
123 2020) and E484Q mutations (Ferreira et al., 2021) can contribute to the resistance
124 to NAbs. In fact, recent studies have shown that the B.1.617.1 variant is resistant to
125 the vaccine-induced NAbs (Edara et al., 2021; Liu et al., 2021a). In contrast to these
126 two sublineages, the B.1.617.2 lineage possesses a unique mutation, T478K. A
127 study has recently shown that the B.1.617.2 variant is also relatively resistant to the
128 NAbs elicited by vaccination (Wall et al., 2021).
129 Interestingly, the P681R mutation in the S protein of B.1.617 lineage is a
130 unique and newly identified mutation in the VOCs so far. Because the P681R
131 mutation is located in the proximity of the furin cleavage site (FCS; residues RRAR
132 positioned between 682-5) of the SARS-CoV-2 S protein (Shang et al., 2020), it is
133 possible that this substitution affects viral replication dynamics and potentially
134 determine the virological characteristics of the B.1.617 variants. In fact, recent
135 investigations have revealed that the deletion of FCS modulates viral replication
136 kinetics in *in vitro* cell cultures and *in vivo* animal models (Johnson et al., 2021;
137 Peacock et al., 2021). However, it remains unclear which mutation(s) are responsible
138 for the virological feature of this newly emerging VOC. In this study, we show that
139 the P681R mutation enhances the cleavage of SARS-CoV-2 S protein. We further
140 demonstrate that the P681R mutation enhances and accelerates viral fusion and
141 promotes cell-cell infection.

Results

Phylogenetic and epidemic dynamics of the B.1.617 lineage

We set out to investigate the phylogenetic relationship of the three subvariants belonging to the B.1.617 lineage. We downloaded 1,761,037 SARS-CoV-2 genomes and information data from the Global Initiative on Sharing All Influenza Data (GISAID) database (https://www.gisaid.org; as of May 31, 2021). As expected, each of three sublineages, B.1.617.1, B.1.617.2 and B.1.617.3, formed a monophyletic cluster, respectively (**Figure 1A**). We then analyzed the epidemic of each of three B.1.617 sublineages. The B.1.617 variant, particularly B.1.617.1, was first detected in India on December 1, 2020 (GISAID ID: EPI_ISL_1372093) (**Figures 1B-1D**). Note that a SARS-CoV-2 variant (GISAID ID: EPI_ISL_2220643) isolated in Texas, the USA, on August 10, 2020, was also recorded to belong to the B.1.617.1. However, the S protein of this viral sequence (GISAID ID: EPI_ISL_2220643) possesses neither L452R nor P681R mutations, both of which are the features of the B.1.617 lineage. Therefore, the EPI_ISL_2220643 sequence isolated in the USA may not be the ancestor of the current B.1.617.1 lineage, and the EPI_ISL_1372093 sequence obtained in India would be the oldest B.1.617 lineage.

The B.1.617.2 (GISAID ID: EPI_ISL_2131509) and B.1.617.3 (GISAID IDs: EPI_ISL_1703672, EPI_ISL_1703659, EPI_ISL_1704392) were detected in India on December 10, 2020 and February 13, 2021, respectively (**Figures 1E and 1F**). The B.1.617.1 sublineage has peaked during February to April, 2021, in India, and then decreased (**Figure 1D**). Although the B.1.617.3 variant has sporadically detected in India (**Figure 1F**), the B.1.617.2 lineage has become dominant in India since March 2021 and spread all over the world (**Figure 1E**). At the end of May 2021, 100%, 70% and 43.3% of the deposited sequences in GISAID per day from India (May 7), the UK (May 21) and the whole world (May 19) have been occupied by the B.1.617.2 sublineage (**Figure 1E and Table S1**).

We next investigated the proportion of amino acid replacements in the S protein of each B.1.617 sublineage comparing with the reference strain (Wuhan-Hu-1; GenBank accession no. NC_045512.2). As shown in **Figure 1G**, the L452R and P681R mutations were highly conserved in the B.1.617 lineage, and notably, the P681R mutation (16,650/16,759 sequences, 99.3%) was the most representative mutation in this lineage. These data suggest that that the P681R mutation is a hallmark of the B.1.617 lineage.

Prominent syncytia formation by the B.1.617 variants

To investigate the virological characteristics of the B.1.617 variants, we conducted virological experiments using two viral isolates of B.1.617.1 (GISAID ID:

180 EPI_ISL_2378733) and B.1.617.2 (GISAID ID: EPI_ISL_2378732) as well as a
181 D614G-bearing B.1.1 isolate (GISAID ID: EPI_ISL_479681) in Japan. In Vero cells,
182 the growth of the B.1.617.1 and B.1.617.2 variants was significantly lower than that
183 of the B.1.1 isolate (**Figure 2A**). Particularly, the levels of viral RNA of the B.1.617
184 variants at 48 hours postinfection (hpi) were more than 150-fold lower than that of
185 the B.1.1 isolate (**Figure 2A**). On the other hand, although the growth kinetics of
186 these three viruses was relatively comparable in VeroE6/TMPRSS2 cells (**Figure**
187 **2A**), microscopic observations showed that the VeroE6/TMPRSS2 cultures infected
188 with these three viruses form syncytia. Notably, the two B.1.617 viruses formed
189 larger syncytia compared to the B.1.1 virus (**Figure 2B**). By measuring the size of
190 the floating syncytia in the infected VeroE6/TMPRSS2 culture, the syncytia formed
191 by the B.1.617.1 and B.1.617.2 infection were significantly (2.3-fold and 2.7-fold)
192 larger than that by the B.1.1 infection (**Figure 2B**). Immunofluorescence assay
193 further showed that the two B.1.617 viruses form larger syncytia in
194 VeroE6/TMPRSS2 cells compared to the B.1.1 isolate (**Figure 2C**). Altogether,
195 these results suggest that the B.1.617 lineages are feasible for forming syncytia and
196 relatively prefer cell-cell infection compared to the D614G-bearing B.1.1 virus.
197
198 **P681R mutation as the determinant of the promotion and acceleration of S-**
199 **mediated fusion**
200 As shown in **Figure 1G**, the P681R mutation is a unique feature of the B.1.617
201 lineage. Because this mutation is located at the proximity of the FCS of SARS-CoV-
202 2 S protein (Shang et al., 2020), we hypothesized that the P681R mutation is
203 responsible for the preference of cell-cell fusion, which leads to larger syncytia
204 formation, by the B.1.617 lineage. To address this possibility, we generated the
205 P681R-bearing artificial virus by reverse genetics (**Figure 3A**) and preformed
206 virological experiments. As shown in **Figure 3B**, the growth kinetics of the
207 D614G/P681R mutant was significantly lower than that of the D614G mutant in Vero
208 and VeroE6/TMPRSS2 cells. Although the viral RNA level at 72 hpi in
209 VeroE6/TMPRSS2 cells was comparable between these two viruses (**Figure 3B**),
210 the size of floating syncytia in the D614G/P681R mutant-infected culture was
211 significantly larger than that in the D614G mutant-infected culture (**Figure 3C**). This
212 observation well corresponds to that in the culture infected with the B.1.617 variants
213 (**Figure 2B**). Moreover, although the viral RNA levels of these two viruses were
214 comparable in HeLa-ACE2/TMPRSS2 cells (**Figure 3B**), prominent and large
215 syncytia were observed only in the culture infected with the D614G/P681R mutant
216 (**Figure 3C**).These results suggest that the feature of the B.1.617 viruses observed

217 in *in vitro* cell culture experiments, particularly forming larger syncytia (**Figure 2**), is
218 well reproduced by the P681R mutation.
219 To directly investigate the effect of P681R mutation on the cleavage of
220 SARS-CoV-2 S protein, we prepared the HIV-1-based pseudoviruses carrying the
221 P681R mutation. Western blotting of the pseudoviruses prepared showed that the
222 level of cleaved S2 subunit was significantly increased by the P681R mutation
223 (**Figure 4A**), suggesting that the P681R mutation facilitates the furin-mediated
224 cleavage of SARS-CoV-2 S protein. We then performed the single-round
225 pseudovirus infection assay using the target HOS cells with or without TMPRSS2
226 expression. In the absence of TMPRSS2, the infectivity of the P681R/D614G-
227 bearing pseudovirus was comparable to that of the D614G pseudovirus (**Figure 4B,**
228 **left**). In the presence of TMPRSS2, the infectivity of the D614G pseudovirus
229 increased at 5.0-6.3-fold compared to the TMPRSS2-null target cells (**Figure 4B,**
230 **right**). Although the infectivity of the D614G/P681R pseudovirus also was increased
231 by TMPRSS2 expression, it was significantly lower than the infectivity of the D614G
232 pseudovirus (**Figure 4B, right**). These data suggest that the P681R mutation
233 attenuates the infectivity of cell-free virus in the presence of TMPRSS2.
234 We next addressed the effect of P681R mutation on viral fusogenicity by
235 cell-based fusion assay. In the effector cells (i.e., S-expressing cells), although the
236 protein expression level of the D614G/P681R S was comparable to that of the
237 D614G S, the level of the cleaved S2 subunit of the D614G/P681R mutant was
238 significantly higher than that of the D614G S (**Figure 4C**). Consistent with the results
239 in the pseudovirus assay (**Figure 4A**), these results suggest that P681R mutation
240 facilitates the furin-mediated S cleavage. Flow cytometry showed that the surface
241 expression level of the D614G/P681R S was significantly lower than the D614G S
242 (**Figure 4D**). Nevertheless, the cell-based fusion assay using the target cells without
243 TMPRSS2 demonstrated that the D614G/P681R S is 2.1-fold more fusogenic than
244 the D614G S with a statistical significance ($P = 0.0002$ by Welch's t test) (**Figure 4E**).
245 Moreover, a mathematical modeling analysis of the fusion assay data showed that
246 the initial fusion velocity of the D614G/P681R S (0.83 ± 0.03 per hour) is significantly
247 (2.8-fold) faster than that the D614G S (0.30 ± 0.03 per hour; $P = 4.0 \times 10^{-6}$ by
248 Welch's t test) (**Figures 4F and 4G**). These data suggest that the P681R mutation
249 enhances and accelerates the SARS-CoV-2 S-mediated fusion. Furthermore, when
250 we use the target cells with TMPRSS2 expression, both the fusion efficacy (~1.2-
251 fold) and initial fusion velocity (~2.0-fold) were increased in both the D614G and
252 D614G/P681R S proteins (**Figures 4F and 4G**). These results suggest that
253 TMPRSS2 facilitates the fusion mediated by SARS-CoV-2 S and human ACE2,

254 while the TMPRSS2-dependent acceleration and promotion of viral fusion is not
255 specific for the P681R mutant.
256
257 **Resistance to NAb-mediated antiviral immunity by the P681R mutation**
258 The resistance to the NAb in the sera of COVID-19 convalescents and vaccinated
259 individuals is a hallmark characteristic of the VOCs [reviewed in (Corti et al., 2021;
260 Harvey et al., 2021)], and Liu et al. and Wall et al. recently showed that the B.1.617.1
261 (Liu et al., 2021a) and B.1.617.2 (Wall et al., 2021) variants are relatively resistant
262 to the NAbs elicited by the BNT162b2 vaccination. To ask whether the P681R
263 mutation contributes to this virological phenotype, we performed the neutralizing
264 assay. As shown in **Figure 5A**, the D614G/P681R pseudovirus was partially (1.2-
265 1.5-fold) resistant to the three monoclonal antibodies targeting the RBD of SARS-
266 CoV-2 S protein. Additionally, the neutralizing experiments using the 19 sera of
267 second BNT162b2 vaccination showed that the D614G/P681R pseudovirus is
268 significantly resistant to the vaccine-induced NAbs compared to the D614G
269 pseudovirus ($P < 0.0001$ by Wilcoxon matched-pairs signed rank test; **Figure 5B**
270 **and Figure S2**). These results suggest that the P681R-bearing pseudovirus is
271 relatively resistant to NAbs. In contrast to the neutralizing activity against cell-free
272 viruses, the SARS-CoV-2 S-based fusion assay showed that cell-cell infection is
273 strongly resistant to the NAbs and the insensitivity to the NAbs on cell-cell infection
274 is not dependent on the P681R mutation (**Figure 5C**). Altogether, these findings
275 suggest that the P681R mutation confers the NAbs resistance upon cell-free viral
276 particles and cell-cell infection is resistant to the NAb-mediated antiviral action
277 compared to cell-free infection.

278 **Discussion**

279 It is evident that most VOCs considered so far have acquired mutations in their S
280 proteins, particularly in the RBD and N-terminal domain, to evade NAbs (Corti et al.,
281 2021; Harvey et al., 2021; Piccoli et al., 2020). In sharp contrast, here we
282 demonstrated that the B.1.617 lineage has acquired a unique strategy to facilitate
283 infection and evade antiviral immunity. The P681R mutation that is highly conserved
284 in this lineage enhances the efficacy to viral fusion and further accelerates its speed
285 of action. The P681R-mediated rapid kinetics of viral fusion may attribute to not only
286 immune evasion but also possibly feasible the infection to exposed individuals.

287 Consistent with previous reports (Kruglova et al., 2021; Xia et al., 2020),
288 here we showed that the cell-cell infection mediated by the SARS-CoV-2 S protein
289 is resistant to NAbs. The effect of NAbs against cell-cell infection has been well
290 studied in HIV-1 (*Retroviridae*) infection, and it is well known that cell-cell infection
291 is relatively more resistant to NAbs compared to cell-free infection [reviewed in
292 (Agosto et al., 2015; Dufloo et al., 2018; Sattentau, 2008)]. The resistance of cell-
293 cell spread against NAbs is not limited to HIV-1 but has been observed in the other
294 viruses such as vaccinia virus (*Poxviridae*) (Law et al., 2002) and hepatitis C virus
295 (*Flaviviridae*) (Timpe et al., 2008), suggesting that cell-cell infection is a common
296 strategy for a variety of viruses to evade antiviral humoral immunity. The fact that the
297 B.1.617 variants as well as the P681R mutant efficiently form syncytia and the S
298 P681R mutant accelerates and promotes cell-cell fusion suggests that switching the
299 preference of viral replication mode from cell-free infection to cell-cell infection may
300 be a unique strategy of the B.1.617 variants to evade antiviral immunity.

301 Previous studies have demonstrated the close association of the FCS in
302 the SARS-CoV-2 S protein with viral replication mode and it is dependent on
303 TMPRSS2. Johnson et al. and Peacock et al. showed that the loss of FCS results in
304 the increase of viral replication efficacy in Vero cells while the attenuation of viral
305 growth in the Vero cells expressing TMPRSS2 (Johnson et al., 2021; Peacock et al.,
306 2021). On the contrary, here we showed that the replication efficacy of the B.1.617
307 variants was severely decreased in Vero cells compared to VeroE6/TMPRSS2 cells.
308 Together with previous findings, our data suggest that the furin-mediated cleavage
309 of the SARS-CoV-2 S protein closely associates with the usage of TMPRSS2. On
310 the other hand, both the FCS-deficient (Johnson et al., 2021) and the P681R-
311 mutated pseudoviruses were resistant to the NAb-mediated antiviral effect. These
312 data suggest that the resistance of the viruses harboring mutations around FCS is
313 not dependent on the usage of TMPRSS2 and the tropism of cell-cell infection.

314 Although the P681R mutation is not located in the RBD of SARS-CoV-2 S
315 protein, the P681R-harboring pseudovirus rendered resistance to the NAbs targeting

316 RBD. Regarding this, the similarity of the evolutionary trajectory of HIV-1 envelope
317 (Env) protein and SARS-CoV-2 S protein has been discussed [reviewed in (Fischer
318 et al., 2021)]. In the case of HIV-1 Env, a type of well studied anti-HIV-1 NAbs (e.g.,
319 2G12, PGT121 and KD-247) targets the variable 3 (V3) region of Env [reviewed in
320 (Sok and Burton, 2018). The Env V3 region is conformationally masked before the
321 binding to viral receptor CD4 and is exposed after receptor binding to proceed viral
322 entry step and determine the tropism of the usage of viral coreceptors [reviewed in
323 (Arrildt et al., 2012)], suggesting that the V3 region is immunodominant and masking
324 the immunodominant epitopes is a strategy for viruses to evade antiviral immunity.
325 In fact, an artificially mutated HIV-1 Env that stably exposes the V3 region can be
326 highly sensitive to the NAbs targeting the V3 region (Hoffman et al., 1999). To
327 overcome the V3-targeting neutralization, HIV-1 Env usually acquires mutations not
328 in the V3 region but in the regions next to the V3 and conformationally masks the
329 epitope in the V3 region (Hatada et al., 2010; Pinter et al., 2005; Pinter et al., 2004;
330 Shibata et al., 2007). Although most NAbs against SARS-CoV-2 target the RBD of
331 S protein (Piccoli et al., 2020), viruses, mainly VOCs, have acquired mutations in
332 this domain (e.g., E484K) to evade neutralization (Baum et al., 2020; Chen et al.,
333 2021; Liu et al., 2021c; Wang et al., 2021b; Weisblum et al., 2020). On the other
334 hand, the P681R mutation is not located in the RBD. Considering the examples of
335 HIV-1 Env studies, the P681R mutation may conformationally mask the
336 immunodominant epitopes located in the RBD to ablate the accessibility of NAb to
337 this domain. Moreover, although the pseudovirus infectivity bearing the P681R
338 mutation was ~2-fold attenuated when the TMPRSS2-expressing cells were used as
339 the target cells, the P681R-bearing pseudovirus exhibited resistance to NAbs.
340 Therefore, the acquisition of this mutation may be due to a trade-off between viral
341 infectivity and immune evasion.
342 In summary, here we demonstrated that the P681R mutation, a hallmark of
343 the B.1.617 lineage, enhances viral fusion and promotes cell-cell infection. Although
344 the P681R mutant is highly fusogenic, the virus harboring the P681R mutation did
345 not necessarily show higher growth compared to the parental virus. Regarding this,
346 the HIV-1 variants with higher fusogenicity have been isolated from AIDS patients,
347 but the enhanced fusogenicity does not promote viral replication in *in vitro* cell
348 cultures (Sterjovski et al., 2007). Similarly, the measles virus (*Paramyxoviridae*)
349 harboring the deficient mutation in viral matrix protein (Cathomen et al., 1998) and
350 substitution mutations in viral fusion protein (Ikegame et al., 2021; Watanabe et al.,
351 2013) are highly fusogenic and efficiently expands via cell-cell fusion. However, the
352 growth kinetics of the mutated measles virus with higher fusogenicity in *in vitro* cell
353 cultures is less efficient than the parental virus (Cathomen et al., 1998). Therefore,

354 the discrepancy between the efficacy of viral growth in *in vitro* cell cultures and viral
355 fusogenicity is not specific for SARS-CoV-2. Rather, the higher fusogenicity is
356 associated with the severity of viral pathogenicity such as HIV-1 encephalitis (Rossi
357 et al., 2008) and fatal subacute sclerosing panencephalitis, which is caused by
358 measles virus infection in brain (Ikegame et al., 2021; Watanabe et al., 2013).
359 Although the association between the COVID-19 severity and/or unusual symptoms
360 caused by SARS-CoV-2 infection and the P681R mutation remains unclear, an early
361 report from the PRE suggests the B.1.617.2 variant, which bears the P681R
362 mutation, may be more pathogenic than the B.1.1.7 lineage (PHE, 2021). Switching
363 viral infection mode by the P681R mutation may relate to the severity and/or unusual
364 outcome of viral infection, therefore, the epidemic of the SARS-CoV-2 variants
365 harboring the P681R mutation should be surveyed in depth.

STAR★METHODS

- KEY RESOURCES TABLE
- RESOURCE AVAILABILITY
    - Lead Contact
    - Materials Availability
    - Data and Code Availability
- EXPERIMENTAL MODEL AND SUBJECT DETAILS
    - Ethics Statement
    - Collection of BNT162b2-Vaccinated Sera
- METHOD DETAILS
    - Viral Genomes
    - Phylogenetic Analyses
    - SARS-CoV-2 Preparation and Titration
    - SARS-CoV-2 Infection
    - Immunofluorescence Staining
    - SARS-CoV-2 Reverse Genetics
    - Real-Time RT-PCR
    - Plasmid Construction
    - Pseudovirus Assay
    - Western blotting
    - SARS-CoV-2 S-Based Fusion Assay
    - Mathematical Modeling for Fusion Velocity Quantification
    - Neutralization Assay
- QUANTIFICATION AND STATISTICAL ANALYSIS

Supplemental Information

Supplemental Information includes 2 figures and 4 tables and can be found with this article online at http://...

Author Contributions

A.S., H.N., K.U., Y.Kosugi, T.Irie, E.P.B., Y.L.T., R.S., K.Shimizu, T.F., R.K., T.Ikeda and K.Sato. performed the experiments.
K.Sadamasu, K.T., T.S., I.Y., H.A., M.N., and K.Y. prepared experimental materials.
J.W. and S.N. performed molecular phylogenetic analysis.
K.Shirakawa, Y.Kazuma, R.N., Y.H., and A.T.-K. collected clinical samples.
A.S., T.Irie, T.F., S.N., T.Ikeda and K.S. designed the experiments and interpreted the results.
K.S. wrote the original manuscript.
All authors reviewed and proofread the manuscript.
The Genotype to Phenotype Japan (G2P-Japan) Consortium contributed to the project administration.

Consortia

The Genotype to Phenotype Japan (G2P-Japan) Consortium: Mika Chiba, Hirotake Furihata, Haruyo Hasebe, Kazuko Kitazato, Haruko Kubo, Naoko Misawa, Nanami Morizako, Akiko Oide, Mai Suganami, Miyoko Takahashi, Kana Tsushima, Miyabishara Yokoyama, Yue Yuan

Acknowledgments

We would like to thank all members belonging to The Genotype to Phenotype Japan (G2P-Japan) Consortium. We thank Dr. Jin Gohda (The University of Tokyo, Japan) for providing reagents. An anti-HIV-1 p24 Monoclonal antibody (clone 183-H12-5C, Cat# ARP-3537) was obtained through the NIH HIV Reagent Program, NIAID, NIH (contributed by Drs. Bruce Chesebro and Kathy Wehrly). The super-computing resource was provided by Human Genome Center at The University of Tokyo and the NIG supercomputer at ROIS National Institute of Genetics.

This study was supported in part by AMED Research Program on Emerging and Re-emerging Infectious Diseases 20fk0108163 (to A.S.), 20fk0108401 (to T.F.), 21fk0108617 (to T.F.), 20fk0108146 (to K.Sato), 20fk0108270 (to K.Sato) and 20fk0108413 (to T.Ikeda, S.N. and K.Sato); AMED Research Program on HIV/AIDS 21fk0410033 (to A.S.) and 21fk0410039 (to K.Sato); AMED Japan Program for Infectious Diseases Research and Infrastructure 20wm0325009 and 21wm0325009 (to A.S.); JST A-STEP JPMJTM20SL (to T.Ikeda); JST SICORP (e-ASIA) JPMJSC20U1 (to K.Sato); JST SICORP JPMJSC21U5 (to K.Sato), JST CREST JPMJCR20H6 (to S.N.) and JPMJCR20H4 (to K.Sato); JSPS KAKENHI Grant-in-Aid for Scientific Research C 19K06382 (to A.S.), 18K07156 (to K.T.) and 21K07060 (to K.T.), Scientific Research B 18H02662 (to K.Sato) and 21H02737 (to K.Sato);

JSPS Fund for the Promotion of Joint International Research (Fostering Joint International Research) 18KK0447 (to K.Sato); JSPS Core-to-Core Program JPJSCCA20190008 (A. Advanced Research Networks) (to K.Sato); JSPS Research Fellow DC1 19J20488 (to I.K.); JSPS Leading Initiative for Excellent Young Researchers (LEADER) (to T.Ikeda); ONO Medical Research Foundation (to K.Sato); Ichiro Kanehara Foundation (to K.Sato); Lotte Foundation (to K.Sato); Mochida Memorial Foundation for Medical and Pharmaceutical Research (to K.Sato); Daiichi Sankyo Foundation of Life Science (to K.Sato); Sumitomo Foundation (to K.Sato); Uehara Foundation (to K.Sato); Takeda Science Foundation (to T.Ikeda and K.Sato); The Tokyo Biochemical Research Foundation (to K.Sato); Mitsubishi Foundation (to T.Ikeda); Shin-Nihon Foundation of Advanced Medical Research (to T.Ikeda); Tsuchiya Foundation (to T.Irie); a Grant for Joint Research Projects of the Research Institute for Microbial Diseases, Osaka University (to A.S.); an intramural grant from Kumamoto University COVID-19 Research Projects (AMABIE) (to T.Ikeda); Intercontinental Research and Educational Platform Aiming for Eradication of HIV/AIDS (to T.Ikeda); and Joint Usage/Research Center program of Institute for Frontier Life and Medical Sciences, Kyoto University (to K.Sato).

449 **References**

450 Agosto, L.M., Uchil, P.D., and Mothes, W. (2015). HIV cell-to-cell transmission:
451 effects on pathogenesis and antiretroviral therapy. Trends Microbiol *23*, 289-295.
452 Arrildt, K.T., Joseph, S.B., and Swanstrom, R. (2012). The HIV-1 env protein: a coat
453 of many colors. Curr HIV/AIDS Rep *9*, 52-63.
454 Baum, A., Fulton, B.O., Wloga, E., Copin, R., Pascal, K.E., Russo, V., Giordano, S.,
455 Lanza, K., Negron, N., Ni, M.*, et al.* (2020). Antibody cocktail to SARS-CoV-2 spike
456 protein prevents rapid mutational escape seen with individual antibodies. Science
457 *369*, 1014-1018.
458 Cathomen, T., Mrkic, B., Spehner, D., Drillien, R., Naef, R., Pavlovic, J., Aguzzi, A.,
459 Billeter, M.A., and Cattaneo, R. (1998). A matrix-less measles virus is infectious and
460 elicits extensive cell fusion: consequences for propagation in the brain. EMBO J *17*,
461 3899-3908.
462 CDC (2021). "SARS-CoV-2 variant classifications and definitions (updated June 10,
463 2021)". https://www.cdc.gov/coronavirus/2019-ncov/variants/variant-info.html.
464 Chen, R.E., Zhang, X., Case, J.B., Winkler, E.S., Liu, Y., VanBlargan, L.A., Liu, J.,
465 Errico, J.M., Xie, X., Suryadevara, N.*, et al.* (2021). Resistance of SARS-CoV-2
466 variants to neutralization by monoclonal and serum-derived polyclonal antibodies.
467 Nat Med *27*, 717-726.
468 Collier, D.A., De Marco, A., Ferreira, I., Meng, B., Datir, R., Walls, A.C., Kemp, S.S.,
469 Bassi, J., Pinto, D., Fregni, C.S.*, et al.* (2021). Sensitivity of SARS-CoV-2 B.1.1.7 to
470 mRNA vaccine-elicited antibodies. Nature *593*, 136-141.
471 Corti, D., Purcell, L.A., Snell, G., and Veesler, D. (2021). Tackling COVID-19 with
472 neutralizing monoclonal antibodies. Cell.
473 Deng, X., Garcia-Knight, M.A., Khalid, M.M., Servellita, V., Wang, C., Morris, M.K.,
474 Sotomayor-González, A., Glasner, D.R., Reyes, K.R., Gliwa, A.S.*, et al.* (2021).
475 Transmission, infectivity, and antibody neutralization of an emerging SARS-CoV-2
476 variant in California carrying a L452R spike protein mutation. Cell *in press*.
477 Dufloo, J., Bruel, T., and Schwartz, O. (2018). HIV-1 cell-to-cell transmission and
478 broadly neutralizing antibodies. Retrovirology *15*, 51.
479 Edara, V.-V., Lai, L., Sahoo, M.K., Floyd, K., Sibai, M., Solis, D., Flowers, M.W.,
480 Hussaini, L., Ciric, C.R., Bechnack, S.*, et al.* (2021). Infection and vaccine-induced
481 neutralizing antibody responses to the SARS-CoV-2 B.1.617.1 variant. BioRxiv,
482 443299.
483 Ferreira, I., Datir, R., Kemp, S., Papa, G., Rakshit, P., Singh, S., Meng, B., Pandey,
484 R., Ponnusamy, K., Radhakrishnan, V.S.*, et al.* (2021). SARS-CoV-2 B.1.617
485 emergence and sensitivity to vaccine-elicited antibodies. BioRxiv, 443253.
486 Fischer, W., Giorgi, E.E., Chakraborty, S., Nguyen, K., Bhattarcharya, T., Theiler, J.,

487 Goloboff, P.A., Yoon, H., Abfalterer, W., Foley, B.T.*, et al.* (2021). HIV-1 and SARS-
488 CoV-2: patterns in the evolution of two pandemic pathogens. Cell Host Microbe *pre-*
489 *proof*.
490 Garcia-Beltran, W.F., Lam, E.C., St Denis, K., Nitido, A.D., Garcia, Z.H., Hauser,
491 B.M., Feldman, J., Pavlovic, M.N., Gregory, D.J., Poznansky, M.C.*, et al.* (2021).
492 Multiple SARS-CoV-2 variants escape neutralization by vaccine-induced humoral
493 immunity. Cell *184*, 2372-2383 e2379.
494 Harvey, W.T., Carabelli, A.M., Jackson, B., Gupta, R.K., Thomson, E.C., Harrison,
495 E.M., Ludden, C., Reeve, R., Rambaut, A., Consortium, C.-G.U.*, et al.* (2021).
496 SARS-CoV-2 variants, spike mutations and immune escape. Nat Rev Microbiol.
497 Hatada, M., Yoshimura, K., Harada, S., Kawanami, Y., Shibata, J., and Matsushita,
498 S. (2010). Human immunodeficiency virus type 1 evasion of a neutralizing anti-V3
499 antibody involves acquisition of a potential glycosylation site in V2. J Gen Virol *91*,
500 1335-1345.
501 Hoffman, T.L., LaBranche, C.C., Zhang, W., Canziani, G., Robinson, J., Chaiken, I.,
502 Hoxie, J.A., and Doms, R.W. (1999). Stable exposure of the coreceptor-binding site
503 in a CD4-independent HIV-1 envelope protein. Proc Natl Acad Sci U S A *96*, 6359-
504 6364.
505 Hoffmann, M., Arora, P., Gross, R., Seidel, A., Hornich, B.F., Hahn, A.S., Kruger, N.,
506 Graichen, L., Hofmann-Winkler, H., Kempf, A.*, et al.* (2021). SARS-CoV-2 variants
507 B.1.351 and P.1 escape from neutralizing antibodies. Cell *184*, 2384-2393 e2312.
508 Hou, Y.J., Chiba, S., Halfmann, P., Ehre, C., Kuroda, M., Dinnon, K.H., 3rd, Leist,
509 S.R., Schafer, A., Nakajima, N., Takahashi, K.*, et al.* (2020). SARS-CoV-2 D614G
510 variant exhibits efficient replication ex vivo and transmission in vivo. Science *370*,
511 1464-1468.
512 Ikeda, T., Molan, A.M., Jarvis, M.C., Carpenter, M.A., Salamango, D.J., Brown, W.L.,
513 and Harris, R.S. (2019). HIV-1 restriction by endogenous APOBEC3G in the myeloid
514 cell line THP-1. J Gen Virol *100*, 1140-1152.
515 Ikeda, T., Symeonides, M., Albin, J.S., Li, M., Thali, M., and Harris, R.S. (2018). HIV-
516 1 adaptation studies reveal a novel Env-mediated homeostasis mechanism for
517 evading lethal hypermutation by APOBEC3G. PLoS Pathog *14*, e1007010.
518 Ikegame, S., Hashiguchi, T., Hung, C.T., Dobrindt, K., Brennand, K.J., Takeda, M.,
519 and Lee, B. (2021). Fitness selection of hyperfusogenic measles virus F proteins
520 associated with neuropathogenic phenotypes. Proc Natl Acad Sci U S A *118*.
521 Johnson, B.A., Xie, X., Bailey, A.L., Kalveram, B., Lokugamage, K.G., Muruato, A.,
522 Zou, J., Zhang, X., Juelich, T., Smith, J.K.*, et al.* (2021). Loss of furin cleavage site
523 attenuates SARS-CoV-2 pathogenesis. Nature *591*, 293-299.
524 Katoh, K., and Standley, D.M. (2013). MAFFT multiple sequence alignment software

525 version 7: improvements in performance and usability. Mol Biol Evol *30*, 772-780.
526 Kawase, M., Shirato, K., van der Hoek, L., Taguchi, F., and Matsuyama, S. (2012).
527 Simultaneous treatment of human bronchial epithelial cells with serine and cysteine
528 protease inhibitors prevents severe acute respiratory syndrome coronavirus entry. J
529 Virol *86*, 6537-6545.
530 Kondo, N., Miyauchi, K., and Matsuda, Z. (2011). Monitoring viral-mediated
531 membrane fusion using fluorescent reporter methods. Curr Protoc Cell Biol *Chapter*
532 *26*, Unit 26 29.
533 Korber, B., Fischer, W.M., Gnanakaran, S., Yoon, H., Theiler, J., Abfalterer, W.,
534 Hengartner, N., Giorgi, E.E., Bhattacharya, T., Foley, B.*, et al.* (2020). Tracking
535 changes in SARS-CoV-2 spike: evidence that D614G increases infectivity of the
536 COVID-19 virus. Cell *182*, 812-827.
537 Kruglova, N., Siniavin, A., Gushchin, V., and Mazurov, D. (2021). SARS-CoV-2 cell-
538 to-cell infection is resistant to neutralizing antibodies. BioRxiv, 442701.
539 Law, M., Hollinshead, R., and Smith, G.L. (2002). Antibody-sensitive and antibody-
540 resistant cell-to-cell spread by vaccinia virus: role of the A33R protein in antibody-
541 resistant spread. J Gen Virol *83*, 209-222.
542 Liu, J., Liu, Y., Xia, H., Zou, J., Weaver, S.C., Swanson, K.A., Cai, H., Cutler, M.,
543 Cooper, D., Muik, A.*, et al.* (2021a). BNT162b2-elicited neutralization of B.1.617 and
544 other SARS-CoV-2 variants. Nature *accelerated*.
545 Liu, Y., Liu, J., Xia, H., Zhang, X., Fontes-Garfias, C.R., Swanson, K.A., Cai, H.,
546 Sarkar, R., Chen, W., Cutler, M.*, et al.* (2021b). Neutralizing activity of BNT162b2-
547 elicited serum. N Engl J Med *384*, 1466-1468.
548 Liu, Z., VanBlargan, L.A., Bloyet, L.M., Rothlauf, P.W., Chen, R.E., Stumpf, S., Zhao,
549 H., Errico, J.M., Theel, E.S., Liebeskind, M.J.*, et al.* (2021c). Identification of SARS-
550 CoV-2 spike mutations that attenuate monoclonal and serum antibody neutralization.
551 Cell Host Microbe *29*, 477-488 e474.
552 Matsuyama, S., Nao, N., Shirato, K., Kawase, M., Saito, S., Takayama, I., Nagata,
553 N., Sekizuka, T., Katoh, H., Kato, F.*, et al.* (2020). Enhanced isolation of SARS-CoV-
554 2 by TMPRSS2-expressing cells. Proc Natl Acad Sci U S A *117*, 7001-7003.
555 Minh, B.Q., Schmidt, H.A., Chernomor, O., Schrempf, D., Woodhams, M.D., von
556 Haeseler, A., and Lanfear, R. (2020). IQ-TREE 2: New Models and Efficient Methods
557 for Phylogenetic Inference in the Genomic Era. Mol Biol Evol *37*, 1530-1534.
558 Motozono, C., Toyoda, M., Zahradnik, J., Ikeda, T., Saito, A., Tan, T.S., Ngare, I.,
559 Nasser, H., Kimura, I., Uriu, K.*, et al.* (2021). An emerging SARS-CoV-2 mutant
560 evading cellular immunity and increasing viral infectivity. BioRxiv, 438288.
561 Niwa, H., Yamamura, K., and Miyazaki, J. (1991). Efficient selection for high-
562 expression transfectants with a novel eukaryotic vector. Gene *108*, 193-199.

563 Ozono, S., Zhang, Y., Ode, H., Sano, K., Tan, T.S., Imai, K., Miyoshi, K., Kishigami,
564 S., Ueno, T., Iwatani, Y.*, et al.* (2021). SARS-CoV-2 D614G spike mutation increases
565 entry efficiency with enhanced ACE2-binding affinity. Nat Commun *12*, 848.
566 Ozono, S., Zhang, Y., Tobiume, M., Kishigami, S., and Tokunaga, K. (2020). Super-
567 rapid quantitation of the production of HIV-1 harboring a luminescent peptide tag. J
568 Biol Chem *295*, 13023-13030.
569 Peacock, T.P., Goldhill, D.H., Zhou, J., Baillon, L., Frise, R., Swann, O.C.,
570 Kugathasan, R., Penn, R., Brown, J.C., Sanchez-David, R.Y.*, et al.* (2021). The furin
571 cleavage site in the SARS-CoV-2 spike protein is required for transmission in ferrets.
572 Nat Microbiol.
573 PHE (2021). Public Health England. "3 June 2021 Risk assessment for SARS-CoV-
574 2 variant: Delta (VOC-21APR-02, B.1.617.2)"
575 https://assets.publishing.service.gov.uk/government/uploads/system/uploads/attac
576 hment_data/file/991135/3_June_2021_Risk_assessment_for_SARS-CoV-
577 2_variant_DELTA.pdf.
578 Piccoli, L., Park, Y.J., Tortorici, M.A., Czudnochowski, N., Walls, A.C., Beltramello,
579 M., Silacci-Fregni, C., Pinto, D., Rosen, L.E., Bowen, J.E.*, et al.* (2020). Mapping
580 Neutralizing and Immunodominant Sites on the SARS-CoV-2 Spike Receptor-
581 Binding Domain by Structure-Guided High-Resolution Serology. Cell *183*, 1024-
582 1042 e1021.
583 Pinter, A., Honnen, W.J., D'Agostino, P., Gorny, M.K., Zolla-Pazner, S., and Kayman,
584 S.C. (2005). The C108g epitope in the V2 domain of gp120 functions as a potent
585 neutralization target when introduced into envelope proteins derived from human
586 immunodeficiency virus type 1 primary isolates. J Virol *79*, 6909-6917.
587 Pinter, A., Honnen, W.J., He, Y., Gorny, M.K., Zolla-Pazner, S., and Kayman, S.C.
588 (2004). The V1/V2 domain of gp120 is a global regulator of the sensitivity of primary
589 human immunodeficiency virus type 1 isolates to neutralization by antibodies
590 commonly induced upon infection. J Virol *78*, 5205-5215.
591 Planas, D., Bruel, T., Grzelak, L., Guivel-Benhassine, F., Staropoli, I., Porrot, F.,
592 Planchais, C., Buchrieser, J., Rajah, M.M., Bishop, E.*, et al.* (2021). Sensitivity of
593 infectious SARS-CoV-2 B.1.1.7 and B.1.351 variants to neutralizing antibodies. Nat
594 Med *27*, 917-924.
595 Plante, J.A., Liu, Y., Liu, J., Xia, H., Johnson, B.A., Lokugamage, K.G., Zhang, X.,
596 Muruato, A.E., Zou, J., Fontes-Garfias, C.R.*, et al.* (2020). Spike mutation D614G
597 alters SARS-CoV-2 fitness. Nature.
598 Plante, J.A., Mitchell, B.M., Plante, K.S., Debbink, K., Weaver, S.C., and Menachery,
599 V.D. (2021). The variant gambit: COVID's next move. Cell Host Microbe *29*, 508-
600 515.

601 Rausch, T., Fritz, M.H., Untergasser, A., and Benes, V. (2020). Tracy: basecalling,
602 alignment, assembly and deconvolution of sanger chromatogram trace files. BMC
603 Genomics *21*, 230.
604 Reed, L.J., and Muench, H. (1938). A Simple Method of Estimating Fifty Percent
605 Endpoints. Am J Hygiene *27*, 493-497.
606 Rossi, F., Querido, B., Nimmagadda, M., Cocklin, S., Navas-Martin, S., and Martin-
607 Garcia, J. (2008). The V1-V3 region of a brain-derived HIV-1 envelope glycoprotein
608 determines macrophage tropism, low CD4 dependence, increased fusogenicity and
609 altered sensitivity to entry inhibitors. Retrovirology *5*, 89.
610 Sattentau, Q. (2008). Avoiding the void: cell-to-cell spread of human viruses. Nat
611 Rev Microbiol *6*, 815-826.
612 Shang, J., Wan, Y., Luo, C., Ye, G., Geng, Q., Auerbach, A., and Li, F. (2020). Cell
613 entry mechanisms of SARS-CoV-2. Proc Natl Acad Sci U S A *117*, 11727-11734.
614 Shema Mugisha, C., Vuong, H.R., Puray-Chavez, M., Bailey, A.L., Fox, J.M., Chen,
615 R.E., Wessel, A.W., Scott, J.M., Harastani, H.H., Boon, A.C.M.*, et al.* (2020). A
616 simplified quantitative real-time PCR assay for monitoring SARS-CoV-2 growth in
617 cell culture. mSphere *5*.
618 Shibata, J., Yoshimura, K., Honda, A., Koito, A., Murakami, T., and Matsushita, S.
619 (2007). Impact of V2 mutations on escape from a potent neutralizing anti-V3
620 monoclonal antibody during in vitro selection of a primary human immunodeficiency
621 virus type 1 isolate. J Virol *81*, 3757-3768.
622 Singh, J., Rahman, S.A., Ehtesham, N.Z., Hira, S., and Hasnain, S.E. (2021). SARS-
623 CoV-2 variants of concern are emerging in India. Nat Med.
624 Sok, D., and Burton, D.R. (2018). Recent progress in broadly neutralizing antibodies
625 to HIV. Nat Immunol *19*, 1179-1188.
626 Sterjovski, J., Churchill, M.J., Ellett, A., Gray, L.R., Roche, M.J., Dunfee, R.L., Purcell,
627 D.F., Saksena, N., Wang, B., Sonza, S.*, et al.* (2007). Asn 362 in gp120 contributes
628 to enhanced fusogenicity by CCR5-restricted HIV-1 envelope glycoprotein variants
629 from patients with AIDS. Retrovirology *4*, 89.
630 Sultana, T., Mamede, J.I., Saito, A., Ode, H., Nohata, K., Cohen, R., Nakayama,
631 E.E., Iwatani, Y., Yamashita, M., Hope, T.J.*, et al.* (2019). Multiple Pathways To
632 Avoid Beta Interferon Sensitivity of HIV-1 by Mutations in Capsid. J Virol *93*.
633 Timpe, J.M., Stamataki, Z., Jennings, A., Hu, K., Farquhar, M.J., Harris, H.J.,
634 Schwarz, A., Desombere, I., Roels, G.L., Balfe, P.*, et al.* (2008). Hepatitis C virus
635 cell-cell transmission in hepatoma cells in the presence of neutralizing antibodies.
636 Hepatology *47*, 17-24.
637 Torii, S., Ono, C., Suzuki, R., Morioka, Y., Anzai, I., Fauzyah, Y., Maeda, Y., Kamitani,
638 W., Fukuhara, T., and Matsuura, Y. (2021). Establishment of a reverse genetics

639 system for SARS-CoV-2 using circular polymerase extension reaction. Cell Rep *35*,
640 109014.
641 Volz, E., Hill, V., McCrone, J.T., Price, A., Jorgensen, D., O'Toole, A., Southgate, J.,
642 Johnson, R., Jackson, B., Nascimento, F.F.*, et al.* (2021). Evaluating the effects of
643 SARS-CoV-2 spike mutation D614G on transmissibility and pathogenicity. Cell *184*,
644 64-75 e11.
645 Wall, E.C., Wu, M., Harvey, R., Kelly, G., Warchal, S., Sawyer, C., Daniels, R.,
646 Hobson, P., Hatipoglu, E., Ngai, Y.*, et al.* (2021). Neutralising antibody activity
647 against SARS-CoV-2 VOCs B.1.617.2 and B.1.351 by BNT162b2 vaccination.
648 Lancet.
649 Wang, P., Casner, R.G., Nair, M.S., Wang, M., Yu, J., Cerutti, G., Liu, L., Kwong,
650 P.D., Huang, Y., Shapiro, L.*, et al.* (2021a). Increased resistance of SARS-CoV-2
651 variant P.1 to antibody neutralization. Cell Host Microbe *29*, 747-751 e744.
652 Wang, P., Nair, M.S., Liu, L., Iketani, S., Luo, Y., Guo, Y., Wang, M., Yu, J., Zhang,
653 B., Kwong, P.D.*, et al.* (2021b). Antibody resistance of SARS-CoV-2 variants B.1.351
654 and B.1.1.7. Nature *593*, 130-135.
655 Watanabe, S., Shirogane, Y., Suzuki, S.O., Ikegame, S., Koga, R., and Yanagi, Y.
656 (2013). Mutant fusion proteins with enhanced fusion activity promote measles virus
657 spread in human neuronal cells and brains of suckling hamsters. J Virol *87*, 2648-
658 2659.
659 Weisblum, Y., Schmidt, F., Zhang, F., DaSilva, J., Poston, D., Lorenzi, J.C.,
660 Muecksch, F., Rutkowska, M., Hoffmann, H.H., Michailidis, E.*, et al.* (2020). Escape
661 from neutralizing antibodies by SARS-CoV-2 spike protein variants. Elife *9*.
662 WHO (2021a). "Coronavirus disease 2019".
663 https://www.who.int/emergencies/diseases/novel-coronavirus-2019.
664 WHO (2021b). "Tracking SARS-CoV-2 variants".
665 https://www.who.int/en/activities/tracking-SARS-CoV-2-variants/.
666 Wu, F., Zhao, S., Yu, B., Chen, Y.M., Wang, W., Song, Z.G., Hu, Y., Tao, Z.W., Tian,
667 J.H., Pei, Y.Y.*, et al.* (2020). A new coronavirus associated with human respiratory
668 disease in China. Nature *579*, 265-269.
669 Xia, S., Liu, M., Wang, C., Xu, W., Lan, Q., Feng, S., Qi, F., Bao, L., Du, L., Liu, S.,
670 *et al.* (2020). Inhibition of SARS-CoV-2 (previously 2019-nCoV) infection by a highly
671 potent pan-coronavirus fusion inhibitor targeting its spike protein that harbors a high
672 capacity to mediate membrane fusion. Cell Res *30*, 343-355.
673 Yurkovetskiy, L., Wang, X., Pascal, K.E., Tomkins-Tinch, C., Nyalile, T.P., Wang, Y.,
674 Baum, A., Diehl, W.E., Dauphin, A., Carbone, C.*, et al.* (2020). Structural and
675 functional analysis of the D614G SARS-CoV-2 spike protein variant. Cell *183*, 739-
676 751 e738.

677 Zhou, B., Thi Nhu Thao, T., Hoffmann, D., Taddeo, A., Ebert, N., Labroussaa, F.,
678 Pohlmann, A., King, J., Steiner, S., Kelly, J.N.*, et al.* (2021). SARS-CoV-2 spike
679 D614G change enhances replication and transmission. Nature *592*, 122-127.
680 Zhou, P., Yang, X.L., Wang, X.G., Hu, B., Zhang, L., Zhang, W., Si, H.R., Zhu, Y.,
681 Li, B., Huang, C.L.*, et al.* (2020). A pneumonia outbreak associated with a new
682 coronavirus of probable bat origin. Nature *579*, 270-273.
683

Figures

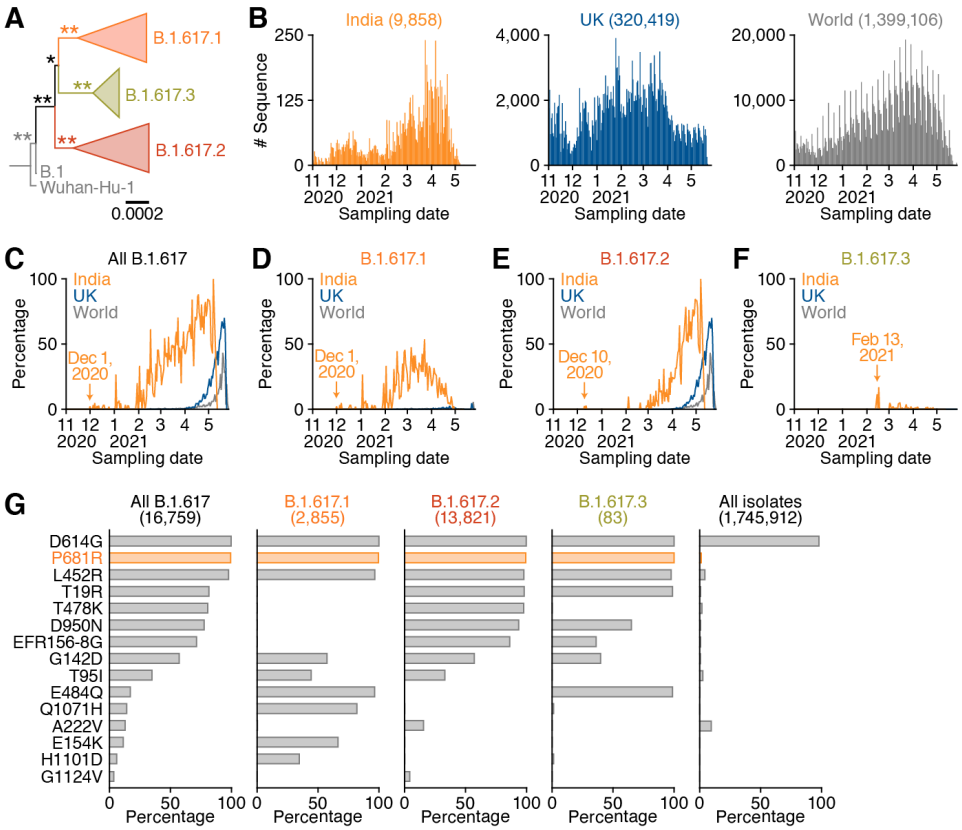

Figure 1. Molecular phylogenetic and epidemic dynamics of the B.1.617 lineage during the pandemic

(**A**) A phylogenetic tree of the B.1.617 lineage. Bar, 0.0002 substitutions per site. Bootstrap values, **, 100%; *, >70%. The uncollapsed tree is shown in **Figure S1**.

(**B-F**) Epidemic dynamics of the B.1.617 lineage. (**B**) The numbers of sequences deposited in GISAID per day for India (orange, left), UK (blue, middle), and the whole world (gray, right). (**C-F**) The percentages of each lineage deposited per day (**C**, all B.1.617; **D**, B.1.617.1; **E**, B.1.617.2; **F**, B.1.617.3) from India (orange), the UK (blue) and the whole world (gray) are shown. The date first identified is indicated. The raw data are summarized in **Table S1**.

(**G**) Proportion of amino acid replacements in the B.1.617 lineage. The top 15 replacements conserved in the S protein of the B.1.617 and its sublineages are summarized. The number in parenthesis indicates the number of sequences included in each panel. The raw data are summarized in **Table S2**.

See also **Figure S1** and **Tables S1 and S2**.

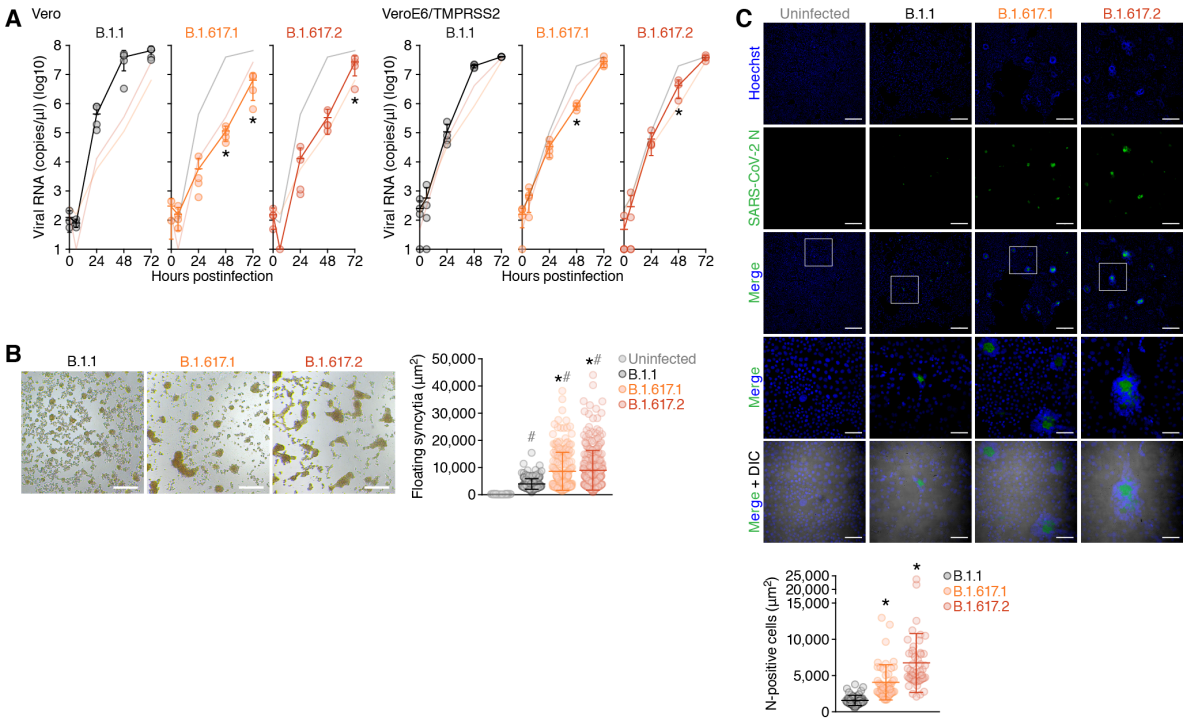

Figure 2. Virological features of the B.1.617 lineage

(**A**) Growth kinetics of two B.1.617 variants and a B.1.1 isolate. Two viral isolates of B.1.617.1 (GISAID ID: EPI_ISL_2378733) and B.1.617.2 (GISAID ID: EPI_ISL_2378732) and a D614G-bearing B.1.1 isolate (GISAID ID: EPI_ISL_479681) [100 50% tissue culture infectious dose ($TCID_{50}$)] were inoculated into Vero cells, VeroE6/TMPRSS2 cells and the copy number of viral RNA in the culture supernatant was quantified by real-time RT-PCR. The growth curves of the viruses inoculated are shown. Assays were performed in quadruplicate.

(**B**) Syncytia formation. The syncytia in infected VeroE6/TMPRSS2 cells were observed at 72 hours postinfection (hpi). (Left) Representative bright-field images of VeroE6/TMPRSS2 cells at 72 hpi are shown. Bars, 100 μm. (Right) The size of floating syncytia in B.1.1-infected (n = 217), B.1.617.1-infected (n = 306) and B.1.617.2-infected (n = 217) cultures are shown. The size of the floating single cells in uninfected culture (n = 177) was also shown as a negative control.

(**C**) Immunofluorescence staining. VeroE6/TMPRSS2 cells infected with the viruses indicated [multiplicity of infection (MOI) 0.01] were stained with anti-SARS-CoV-2 nucleocapsid (N) (green) and DAPI (blue). (Top) Representative images at 48 hpi are shown. Areas enclosed with squares are enlarged in the bottom panels. DIC, differential interference contrast. Bars, 200 μm for low magnification panels; 50 μm for high magnification panels. (Bottom) The area of N-positive cells in B.1.1-infected (n = 50), B.1.617.1-infected (n = 50) and B.1.617.2-infected (n = 50) cultures are shown.

725 In **A**, statistically significant differences (*, $P < 0.05$) versus the B.1.1 isolate were
726 determined by Student's *t* test.
727 In **B and C**, statistically significant differences versus the B.1.1-infected culture (*, P
728 < 0.05) and uninfected culture (#, $P < 0.05$) were determined by the Mann-Whitney
729 U test.

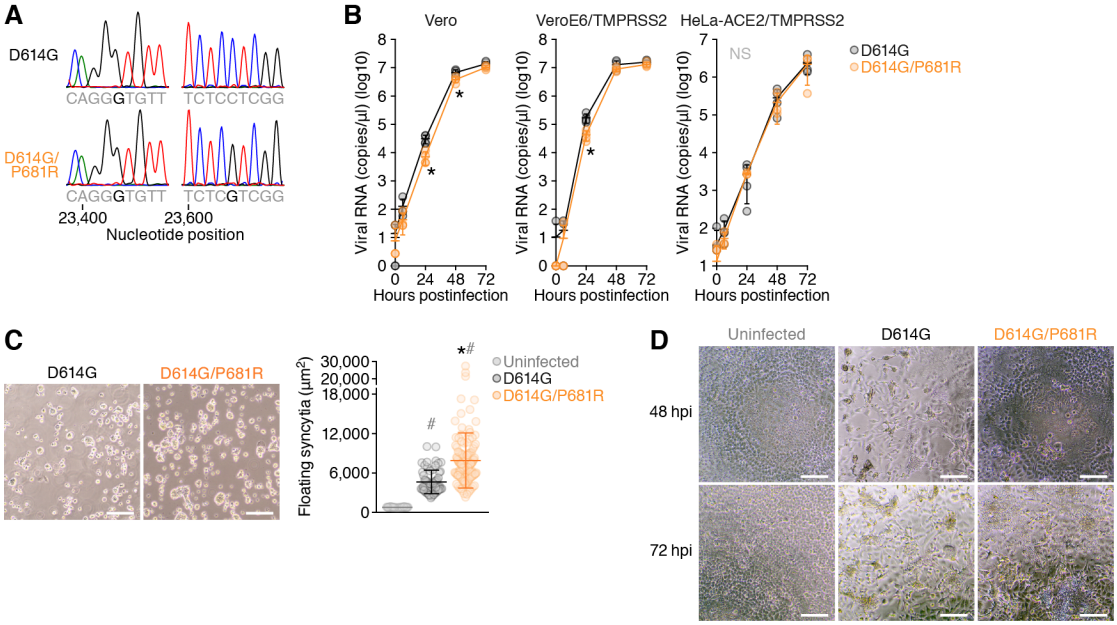

Figure 3. Virological features of the P681R-harboring virus

(**A**) Chromatograms of the mutated regions of SARS-CoV-2 viruses artificially generated by reverse genetics. Chromatograms of nucleotide positions 23,399-23,407 (left) and 23,600-23,609 (right) of parental SARS-CoV-2 (strain WK-521, PANGO lineage A; GISAID ID: EPI_ISL_408667) and the D614G (A23403G in nucleotide) and P681R (C23604G in nucleotide) mutation are shown.

(**B**) Growth kinetics of artificially generated viruses. The D614G and D614G/P681R mutant viruses were generated by reverse genetics. These viruses (100 $TCID_{50}$) were inoculated into Vero cells, VeroE6/TMPRSS2 cells, and HeLa-ACE2/TMPRSS2 cells and the copy number of viral RNA in the culture supernatant was quantified by real-time RT-PCR. The growth curves of the viruses inoculated are shown. Assays were performed in quadruplicate.

(**C and D**) Syncytia formation. The floating syncytia in infected VeroE6/TMPRSS2 cells at 72 hpi (**C**) and the adherent syncytia in infected HeLa-ACE2/TMPRSS2 at 48 hpi (**D**) are shown. In **C**, The size of floating syncytia in the D614G mutant-infected (n = 63) and the D614G/P681R mutant-infected (n = 126) cultures are shown. The size of the floating single cells in uninfected culture (n = 60) was also shown as a negative control. Bars, 100 μm.

In **B**, statistically significant differences (*, $P < 0.05$) versus the D614G virus were determined by Student's *t* test.

In **C**, statistically significant differences versus the D614G mutant-infected culture (*, $P < 0.05$) and uninfected culture (#, $P < 0.05$) were determined by the Mann-Whitney U test.

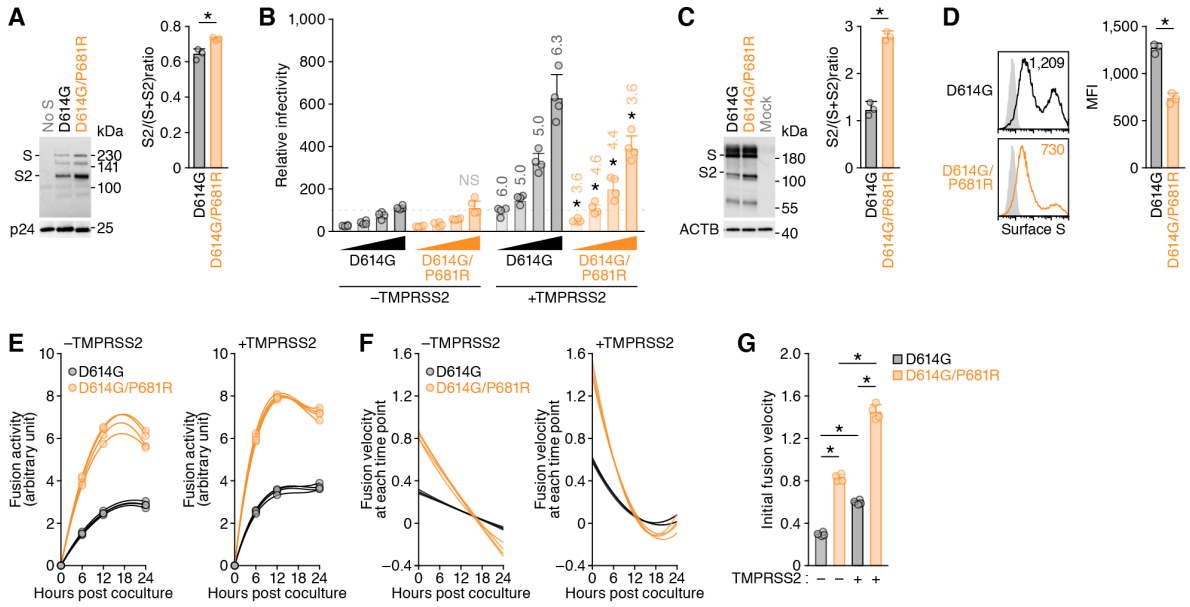

Figure 4. Promotion of cell-cell fusion by the P681R mutation

(**A**) Western blotting of pseudoviruses. (Left) Representative blots of SARS-CoV-2 full-length S and cleaved S2 proteins as well as HIV-1 p24 capsid as an internal control. kDa, kilodalton. (Right) The ratio of S2 to the full-length S plus S2 proteins on pseudovirus particles.

(**B**) Pseudovirus assay. The HIV-1-based reporter virus pseudotyped with the SARS-CoV-2 S D614G or D614G/P681R was inoculated into HOS-ACE2 cells or HOS-ACE2/TMPRSS2 cells at 4 different doses (2.5× 10^5, 5.0 × 10^5, 1 × 10^6 and 2 × 10^6 HiBiT values). Percentages of infectivity compared to the virus pseudotyped with parental S D614G (2 × 10^6 HiBiT values) in HOS-ACE2 cells are shown. The numbers on the bars of the HOS-ACE2/TMPRSS2 cell data indicate the fold change versus the HOS-ACE2 cell data. Assays were performed in quadruplicate.

(**C**) Western blotting of the S-expressing cells. (Left) Representative blots of SARS-CoV-2 full-length S and cleaved S2 proteins as well as ACTB as an internal control. kDa, kilodalton. (Right) The ratio of S2 to the full-length S plus S2 proteins in the S-expressing cells.

(**D**) Flow cytometry of the S-expressing cells. (Left) Representative histogram of the S protein expression on the cell surface. The number in the histogram indicates the mean fluorescence intensity (MFI). (Right) The MFI of surface S on the S-expressing cells.

(**E-G**) SARS-CoV-2 S-based fusion assay. Effector cells (S-expressing cells) and target cells (ACE2-expressing cells or ACE2/TMPRSS2-expressing cells) were prepared, and the fusion activity was measured as described in **STAR★METHODS**.

(**E**) Kinetics of fusion activity (experimental data). Assays were performed in

779 quadruplicate, and fusion activity (arbitrary unit) is shown. (**F and G**) The kinetics
780 of fusion velocity estimated by a mathematical model based on the kinetics of fusion
781 activity data (see **STAR★METHODS**). (**G**) Initial velocity of the S-mediated fusion.
782 In **B, D, and E**, statistically significant differences (*, $P < 0.05$) versus the D614G S
783 were determined by Student's *t* test.
784 In **F and G,** statistically significant differences (*, $P < 0.05$) versus the D614G S were
785 determined by two-sided Welch's *t* test.

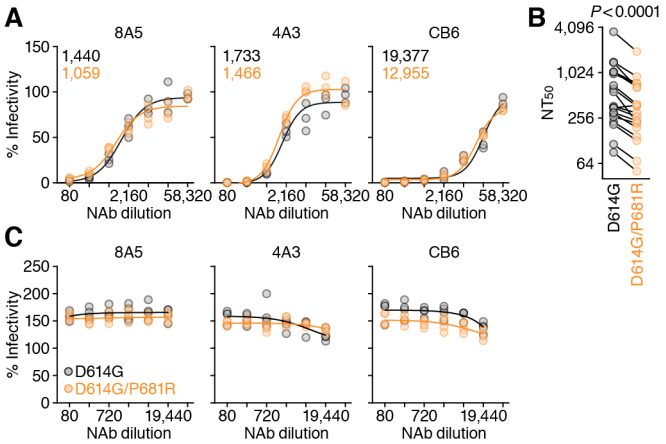

Figure 5. Association of the P681R mutation on the sensitivity to NAbs

Neutralization assay was performed by using three RBD-targeting monoclonal antibodies (clones 8A5, 4A3 and CB6) (**A and C**) and 19 vaccinated sera (**B**). NAbs were used for the pseudovirus assay (**A and B**) and the S-based fusion assay (**C**). Pseudoviruses and effector cells (S-expressing cells) were treated with serially diluted NAbs or sera as described in **STAR★METHODS**. The raw data of **B** is shown in **Figure S2**. NT_{50}, 50% neutralization titer.

In **A**, the NT_{50} values of the D614G S (black) and D614G/P681R S (orange) are indicated.

In **B**, a statistically significant difference versus the D614G virus was determined by Wilcoxon matched-pairs signed rank test.

See also **Figure S2**.

799 **Table S1.** Number of daily deposited sequences in GISAID, related to Figure 1
800
801 **Table S2.** Percentage of the mutations detected in the S protein of the B.1.617
802 lineage, related to Figure 1
803
804 **Table S3.** The SARS-CoV-2 genomic region encoded by each template and the
805 primers used for the preparation of each fragment for CPER, related to Figure 2
806
807 **Table S4.** Primers used for the preparation of the expression plasmids for mutated
808 SARS-CoV-2 S proteins, related to Figure 4
809

STAR★METHODS

KEY RESOURCES TABLE

RESOURCE AVAILABILITY

Lead Contact

Further information and requests for resources and reagents should be directed to and will be fulfilled by the Lead Contact, Kei Sato (KeiSato@g.ecc.u-tokyo.ac.jp).

Materials Availability

All unique reagents generated in this study are listed in the Key Resources Table and available from the Lead Contact with a completed Materials Transfer Agreement.

Data and Code Availability

Additional Supplemental Items are available from Mendeley Data at http://...

EXPERIMENTAL MODEL AND SUBJECT DETAILS

Ethics Statement

For virus isolation, this study was approved by the Institutional Review Board of Tokyo Metropolitan Institute of Public Health, according to the Declaration of Helsinki 2013 (approval number 3KenKenKen-466). For the use of human specimen, all protocols involving human subjects recruited at Kyoto University were reviewed and approved by the Institutional Review Boards of Kyoto University (approval number G0697). All human subjects provided written informed consent.

Collection of BNT162b2-Vaccinated Sera

Peripheral blood were collected four weeks after the second vaccination of BNT162b2 (Pfizer-BioNTech), and the sera of 19 vaccinees (average age: 38, range: 28-59, 26% male) were isolated from peripheral blood. Sera were inactivated at 56°C for 30 min and stored at –80°C until use.

Cell Culture

HEK293 cells (a human embryonic kidney cell line; ATCC CRL-1573), HEK293T cells (a human embryonic kidney cell line; ATCC CRL-3216), and HOS cells (a human osteosarcoma cell line; ATCC CRL-1543) were maintained in Dulbecco's modified Eagle's medium (high glucose) (Wako, Cat# 044-29765) containing 10% fetal bovine serum (FBS) and 1% PS.

HOS-ACE2/TMPRSS2 cells, the HOS cells stably expressing human ACE2, was prepared as described previously (Ferreira et al., 2021; Ozono et al., 2021).

Vero cells [an African green monkey (*Chlorocebus sabaeus*) kidney cell line; JCRB0111] were maintained in Eagle's minimum essential medium (Wako, Cat# 051-07615) containing 10% FBS and 1% PS.

VeroE6/TMPRSS2 cells [an African green monkey (*Chlorocebus sabaeus*) kidney cell line; JCRB1819] (Matsuyama et al., 2020) were maintained in Dulbecco's modified Eagle's medium (low glucose) (Wako, Cat# 041-29775) containing 10% FBS, G418 (1 mg/ml; Nacalai Tesque, Cat# G8168-10ML) and 1% PS.

HeLa-ACE2-TMPRSS2 cells (JCRB1835 (Kawase et al., 2012) were maintained in Dulbecco's modified Eagle's medium (low glucose) (Sigma-Aldrich, Cat# D6046-500ML) containing 10% FBS, 1 mg/ml G418 and 1% PS.

HEK293-C34 cells, the *IFNAR1* KO HEK293 cells expressing human ACE2 and TMPRSS2 by doxycycline treatment (Torii et al., 2021), were maintained in Dulbecco's modified Eagle's medium (high glucose) (Sigma-Aldrich, Cat# R8758-500ML) containing 10% FBS, 10 μg/ml blasticidin (InvivoGen, Cat# ant-bl-1) and 1% PS.

METHOD DETAILS

Viral Genomes

All SARS-CoV-2 genome sequences and annotation information used in this study were downloaded from GISAID (https://www.gisaid.org) as of May 31, 2021 (1,761,037 sequences). We first excluded the genomes with non-human hosts. We obtained SARS-CoV-2 variants belonging to the B.1.617 lineage based on the PANGO annotation (i.e. sublineages B.1.617.1, B.1.617.2, or B.1.617.3) for each sequence in the GISAID metadata. Note that only one variant belonging to the B.1.617 lineage (GISAID ID: EPI_ISL_1544002 isolated in India on February 25, 2021) was not used in the analysis because the variant is not assigned any three sublineages possibly due to 212 undetermined nucleotides in the genome. To infer epidemiology of the B.1.617 lineage (**Figure 1B-1F**), we excluded genomes that sampling date information are not available, and collected 2,855, 13,821, or 83 sequences belonging to the B.1.617.1, B.1.617.2, or B.1.617.3 sublineage, respectively.

Phylogenetic Analyses

To infer the phylogeny of the B.1.617 sublineages, we screened SARS-CoV-2 genomes by removing genomes containing undetermined nucleotides at coding regions. Since the number of genomes belonging to the sublineage B.1.617.1 or

884 B.1.617.2 are large (i.e. 894 or 6152 sequences, respectively), we used 150
885 sequences randomly chosen for each sublineage. For the B.1.617.3 sublineage, 32
886 genomes were used. We used Wuhan-Hu-1 strain isolated in China on December
887 31, 2019 (GenBank ID: NC_045512.2 and GISAID ID: EPI_ISL_402125) and LOM-
888 ASST-CDG1 strain isolated Italy on February 20, 2020 (GISAID ID:
889 EPI_ISL_412973) as an outgroup. We then collected 334 representative SARS-
890 CoV-2 sequences, and aligned entire genome sequences by using the FFT-NS-1
891 program in MAFFT suite v7.407 (Katoh and Standley, 2013). All sites with gaps in
892 alignment are removed, and the total length of alignment is 29,085 nucleotides.
893 Maximum likelihood tree was generated by IQ-TREE 2 v2.1.3 software with 1,000
894 bootstraps (Minh et al., 2020). GTR+G substitution model is utilized based on BIC
895 criterion.
896
897 **SARS-CoV-2 Preparation and Titration**
898 Two viral isolates belonging to the B.1.617 lineage, B.1.617.1 (GISAID ID:
899 EPI_ISL_2378733) and B.1.617.2 (GISAID ID: EPI_ISL_2378732) and a D614G-
900 bearing B.1.1 isolate (GISAID ID: EPI_ISL_479681) were isolated from SARS-CoV-
901 2-positive individuals in Japan. Briefly, 100 µl of the nasopharyngeal swab obtained
902 from SARS-CoV-2-positive individuals were inoculated into VeroE6/TMPRSS2 cells
903 in the biosafety level 3 laboratory. After the incubation at 37°C for 15 minutes, a
904 maintenance medium supplemented with Eagle's minimum essential medium
905 (FUJIFILM Wako Pure Chemical Corporation, Cat# 056-08385) including 2% FBS
906 and 1% PS was added, and the cells were cultured at 37°C under 5% CO_2. The
907 cytopathic effect (CPE) was confirmed under an inverted microscope (Nikon), and
908 the viral load of the culture supernatant in which CPE was observed was confirmed
909 by real-time RT-PCR. To determine viral genome sequences, RNA was extracted
910 from the culture supernatant using QIAamp viral RNA mini kit (Qiagen, Qiagen, Cat#
911 52906) . cDNA library was prepared by using NEB Next Ultra RNA Library Prep Kit
912 for Illumina (New England Biolab, Cat# E7530) and whole genome sequencing was
913 performed by MiSeq (Illumina).
914 To prepare the working virus, 100 µl of the seed virus was inoculated into
915 VeroE6/TMPRSS2 cells (5,000,000 cells in a T-75 flask). At one hour after infection,
916 the culture medium was replaced with Dulbecco's modified Eagle's medium (low
917 glucose) (Wako, Cat# 041-29775) containing 2% FBS and 1% PS; at 2-3 days
918 postinfection, the culture medium was harvested and centrifuged, and the
919 supernatants were collected as the working virus.
920 The titer of the prepared working virus was measured as 50% tissue culture
921 infectious dose ($TCID_{50}$). Briefly, one day prior to infection, VeroE6/TMPRSS2 cells

922 (10,000 cells/well) were seeded into a 96-well plate. Serially diluted virus stocks were
923 inoculated to the cells and incubated at 37°C for 3 days. The cells were observed
924 under microscopy to judge the CPE appearance. The value of $TCID_{50}$/ml was
925 calculated with the Reed–Muench method (Reed and Muench, 1938).
926
927 **SARS-CoV-2 Infection**
928 One day prior to infection, Vero cells (10,000 cells), VeroE6/TMPRSS2 cells (10,000
929 cells), HeLa-ACE2/TMPRSS2 cells (10,000 cells) were seeded into a 96-well plate.
930 SARS-CoV-2 (100 $TCID_{50}$) was inoculated and incubated at 37°C for 1 h. The
931 infected cells were washed, and 180 µl of culture medium was added. The culture
932 supernatant (10 µl) was harvested at indicated time points and used for real-time
933 RT-PCR to quantify the viral RNA copy number. To monitor the syncytia formed in
934 infected cell culture, the bright-field photos were obtained using ECLIPSE Ts2
935 (Nikon). The size of floating syncytia was measured by "quick selection tool" in
936 Photoshop CS5 (Adobe) as pixel, and the area of floating syncytia was calculated
937 from the pixel value.
938
939 **Immunofluorescence Staining**
940 One day prior to infection, VeroE6/TMPRSS2 cells (200,000 cells) were seeded on
941 the coverslips put in 12-well plate and were infected with SARS-CoV-2 at MOI 0.01.
942 At 48 hours postinfection, the cells were fixed with 4% paraformaldehyde in
943 phosphate buffer saline (PBS) (Nacalai Tesque, Cat# 09154-85) for 10 min at room
944 temperature. The fixed cells were permeabilized with 0.1% Triton X-100 in PBS for
945 10 min, blocked with 10% FBS in PBS for overnight at 4°C, and then stained using
946 mouse anti-SARS-CoV-2 N monoclonal antibody (GeneTex, Cat# GTX632269) for
947 1 h. After washing three times with PBS, cells were incubated with an Alexa 488-
948 conjugated anti-mouse IgG antibody (Jackson ImmunoResearch, Cat# 015-540-
949 003) for 1 h. Nuclei were stained with Hoechst 33342 (Thermo Fisher Scientific, Cat#
950 H3570). The coverslips were mounted on glass slides using Fluoromount-G
951 (Southern Biotechnology, Cat# 0100-01) with Hoechst 33342. Fluorescence
952 microscopy was performed on a confocal laser microscope (A1RSi, Nikon) and
953 captured with NIS-Elements AR software (Nikon). The area of N-positive cells was
954 quantified using Fiji software implemented in Image J.
955
956 **SARS-CoV-2 Reverse Genetics**
957 Recombinant SARS-CoV-2 was generated by circular polymerase extension
958 reaction (CPER) as previously described (Motozono et al., 2021; Torii et al., 2021).
959 In brief, 9 DNA fragments encoding the partial genome of SARS-CoV-2 (strain WK-

960 521, PANGO lineage A; GISAID ID: EPI_ISL_408667) (Matsuyama et al., 2020)
961 were prepared by PCR using PrimeSTAR GXL DNA polymerase (Takara, cat#
962 R050A). A linker fragment encoding hepatitis delta virus ribozyme, bovine growth
963 hormone polyA signal and cytomegalovirus promoter was also prepared by PCR.
964 The corresponding SARS-CoV-2 genomic region and the templates and primers of
965 this PCR are summarized in **Table S3**. The 10 obtained DNA fragments were mixed
966 and used for CPER (Torii et al., 2021).
967 To produce recombinant SARS-CoV-2, the CPER products were
968 transfected into HEK293-C34 cells using TransIT-LT1 (Takara, cat# MIR2300)
969 according to the manufacturer's protocol. At one day posttransfection, the culture
970 medium was replaced with Dulbecco's modified Eagle's medium (high glucose)
971 (Sigma-Aldrich, cat# R8758-500ML) containing 2% FCS, 1% PS and doxycycline (1
972 μg/ml; Takara, cat# 1311N). At six days posttransfection, the culture medium was
973 harvested and centrifuged, and the supernatants were collected as the seed virus.
974 To remove the CPER products (i.e., SARS-CoV-2-related DNA), 1 ml of the seed
975 virus was treated with 2 μl TURBO DNase (Thermo Fisher Scientific, cat# AM2238)
976 and incubated at 37°C for 1 h. Complete removal of the CPER products (i.e., SARS-
977 CoV-2-related DNA) from the seed virus was verified by PCR. The working virus was
978 prepared by using the seed virus as described above.
979 To generate recombinant SARS-CoV-2 mutants, mutations were inserted
980 in fragment 8 (**Table S3**) using the GENEART site-directed mutagenesis system
981 (Thermo Fisher Scientific, cat# A13312) according to the manufacturer's protocol
982 with the following primers: Fragment 8_S D614G forward, 5'-CCA GGT TGC TGT
983 TCT TTA TCA GGG TGT TAA CTG CAC AGA AGT CCC TG-3'; Fragment 8_S
984 D614G reverse, 5'- CAG GGA CTT CTG TGC AGT TAA CAC CCT GAT AAA GAA
985 CAG CAA CCT GG -3'; Fragment 8_S P681R forward, 5'-AGA CTC AGA CTA ATT
986 CTC GTC GGC GGG CAC GTA GTG TA-3'; and Fragment 8_S P681R reverse, 5'-
987 TAC ACT ACG TGC CCG CCG ACG AGA ATT AGT CTG AGT CT-3', according to
988 the manufacturer's protocol. Nucleotide sequences were determined by a DNA
989 sequencing service (Fasmac), and the sequence data were analyzed by
990 Sequencher version 5.1 software (Gene Codes Corporation). The CPER for the
991 preparation of SARS-CoV-2 mutants was performed using mutated fragment 8
992 instead of parental fragment 8. Subsequent experimental procedures correspond to
993 the procedure for parental SARS-CoV-2 preparation (described above). To verify
994 insertion of the mutation in the working viruses, viral RNA was extracted using a
995 QIAamp viral RNA mini kit (Qiagen, cat# 52906) and reverse transcribed using
996 SuperScript III reverse transcriptase (Thermo Fisher Scientific, cat# 18080085)
997 according to the manufacturers' protocols. DNA fragments including the mutations

998 inserted were obtained by RT-PCR using PrimeSTAR GXL DNA polymerase
999 (Takara, cat# R050A) and the following primers: WK-521 23339-23364 forward, 5'-
1000 GGT GGT GTC AGT GTT ATA ACA CCA GG-3'; and WK-521 24089-24114 reverse,
1001 5'-CAA ATG AGG TCT CTA GCA GCA ATA TC-3'. Nucleotide sequences were
1002 determined as described above, and sequence chromatograms (**Figure 2A**) were
1003 visualized using the web application Tracy (https://www.gear-genomics.com/teal/)
1004 (Rausch et al., 2020).
1005
1006 **Real-Time RT-PCR**
1007 Real-time RT-PCR was performed as previously described (Motozono et al., 2021;
1008 Shema Mugisha et al., 2020). Briefly, 5 µl of culture supernatant was mixed with 5
1009 µl of 2 × RNA lysis buffer [2% Triton X-100, 50 mM KCl, 100 mM Tris-HCl (pH 7.4),
1010 40% glycerol, 0.8 U/µl recombinant RNase inhibitor (Takara, cat# 2313B)] and
1011 incubated at room temperature for 10 min. RNase-free water (90 µl) was added, and
1012 the diluted sample (2.5 µl) was used as the template for real-time RT-PCR performed
1013 according to the manufacturer's protocol using the One Step TB Green PrimeScript
1014 PLUS RT-PCR kit (Takara, cat# RR096A) and the following primers: Forward *N*, 5'-
1015 AGC CTC TTC TCG TTC CTC ATC AC-3'; and Reverse *N*, 5'-CCG CCA TTG CCA
1016 GCC ATT C-3'. The copy number of viral RNA was standardized with a SARS-CoV-
1017 2 direct detection RT-qPCR kit (Takara, cat# RC300A). The fluorescent signal was
1018 acquired using a QuantStudio 3 Real-Time PCR system (Thermo Fisher Scientific),
1019 a CFX Connect Real-Time PCR Detection system (Bio-Rad) or a 7500 Real Time
1020 PCR System (Applied Biosystems).
1021
1022 **Plasmid Construction**
1023 A plasmid expressing the SARS-CoV-2 S D614G protein was prepared in our
1024 previous study (Ozono et al., 2021). A plasmid expressing the SARS-CoV-2
1025 D614G/P681R S protein (pC-S-D614G/P681R) was generated by site-directed
1026 mutagenesis PCR using pC-SARS2-S D614G (Ozono et al., 2021) as the template
1027 and the following primers listed in **Table S4**. The resulting PCR fragment was
1028 digested with KpnI and NotI and inserted into the KpnI-NotI site of the pCAGGS
1029 vector (Niwa et al., 1991).
1030
1031 **Pseudovirus Assay**
1032 Pseudovirus assay was performed as previously described (Motozono et al., 2021;
1033 Ozono et al., 2021). Briefly, the pseudoviruses, lentivirus (HIV-1)-based, luciferase-
1034 expressing reporter viruses pseudotyped with the SARS-CoV-2 S protein and its
1035 derivatives, HEK293T cells (1 × 10^6 cells) were cotransfected with 1 µg of psPAX2-

1036 IN/HiBiT (Ozono et al., 2020), 1 μg of pWPI-Luc2 (Ozono et al., 2020), and 500 ng
1037 of plasmids expressing parental S or its derivatives using Lipofectamine 3000
1038 (Thermo Fisher Scientific, Cat# L3000015) or PEI Max (Polysciences, Cat# 24765-
1039 1) according to the manufacturer's protocol. At two days posttransfection, the culture
1040 supernatants were harvested, centrifuged. The amount of pseudoviruses prepared
1041 was quantified using the HiBiT assay as previously described (Ozono et al., 2021;
1042 Ozono et al., 2020). The pseudoviruses prepared were stored at –80°C until use.
1043 For the experiment, HOS-ACE2 cells and HOS-ACE2/TMPRSS2 cells (10,000
1044 cells/50 μl) were seeded in 96-well plates and infected with 100 μl of the
1045 pseudoviruses prepared at 4 different doses. At two days postinfection, the infected
1046 cells were lysed with a One-Glo luciferase assay system (Promega, Cat# E6130),
1047 and the luminescent signal was measured using a CentroXS3 plate reader
1048 (Berthhold Technologies) or GloMax explorer multimode microplate reader 3500
1049 (Promega).
1050
1051 **Western blotting**
1052 Western blotting was performed as previously described (Ikeda et al., 2019; Ikeda
1053 et al., 2018; Sultana et al., 2019). To quantify the level of the cleaved S2 protein in
1054 the cells, the harvested cells were washed and lysed in lysis buffer [25 mM HEPES
1055 (pH 7.2), 20% glycerol, 125 mM NaCl, 1% Nonidet P40 substitute (Nalacai Tesque,
1056 Cat# 18558-54), protease inhibitor cocktail (Nalacai Tesque, Cat# 03969-21)]. After
1057 quantification of total protein by protein assay dye (Bio-Rad, Cat# 5000006), lysates
1058 were diluted with 2 × sample buffer [100 mM Tris-HCl (pH 6.8), 4% SDS, 12% β-
1059 mercaptoethanol, 20% glycerol, 0.05% bromophenol blue] and boiled for 10 min.
1060 Ten microliter of the samples (50 μg of total protein) were subjected to western
1061 blotting. To quantify the level of the cleaved S2 protein on virions, 900 μl of the
1062 culture medium including the pseudoviruses were layered onto 500 μl of 20%
1063 sucrose in PBS and centrifuged at 20,000 × g for 2 h at 4°C. Pelleted virions were
1064 resuspended in 1× NuPAGE LDS sample buffer (Thermo Fisher Scientific, Cat#
1065 NP0007) containing 2% β-mercaptoethanol, and the lysed virions were subjected to
1066 western blotting. For the protein detection, following antibodies were used: mouse
1067 anti-SARS-CoV-2 S monoclonal antibody (clone 1A9, GeneTex, Cat# GTX632604),
1068 rabbit anti-ACTB monoclonal antibody (clone 13E5, Cell Signaling, Cat# 4970),
1069 mouse anti-HIV-1 p24 monoclonal antibody (clone 183-H12-5C, obtained from the
1070 HIV Reagent Program, NIH, Cat# ARP-3537), horseradish peroxidase (HRP)-
1071 conjugated donkey anti-rabbit IgG polyclonal antibody (Jackson ImmunoResearch,
1072 Cat# 711-035-152), and HRP-conjugated donkey anti-mouse IgG polyclonal
1073 antibody (Jackson ImmunoResearch, Cat# 715-035-150). Chemiluminescence was

1074 detected using SuperSignal West Femto Maximum Sensitivity Substrate (Thermo
1075 Fisher Scientific, Cat# 34095) or Western BLoT Ultra Sensitive HRP Substrate
1076 (Takara, Cat# T7104A) according to the manufacturers' instruction. Bands were
1077 visualized using the image analyzer, Amersham Imager 600 (GE Healthcare), and
1078 the band intensity was quantified using Image Studio Lite (LI-COR Biosciences) or
1079 Image J.
1080
1081 **SARS-CoV-2 S-Based Fusion Assay**
1082 The SARS-CoV-2 S-based fusion assay was performed as previously described
1083 (Motozono et al., 2021). This assay utilizes a dual split protein (DSP) encoding
1084 *Renilla* luciferase (RL) and *GFP* genes, and the respective split proteins, DSP_{1-7} and
1085 DSP_{8-11}, are expressed in effector and target cells by transfection (Ikeda et al., 2018;
1086 Kondo et al., 2011). Briefly, on day 1, effector cells (i.e., S-expressing cells) and
1087 target cells (i.e., ACE2-expressing cells) were prepared at a density of 0.6 to 0.8 ×
1088 10^6 cells in a 6 well plate. To prepare effector cells, HEK293 cells were cotransfected
1089 with the expression plasmids for D614G S or D614G/P681R (400 ng) with $pDSP_{1-7}$
1090 (400 ng) using TransIT-LT1 (Takara, Cat# MIR2300). To prepare target cells,
1091 HEK293 cells were cotransfected with pC-ACE2 (200 ng) and $pDSP_{8-11}$ (400 ng). In
1092 addition to the plasmids above, selected wells of target cells were also cotransfected
1093 with pC-TMPRSS2 (40 ng). On day 3 (24 h posttransfection), 16,000 effector cells
1094 were detached and reseeded into 96-well black plates (PerkinElmer, Cat# 6005225),
1095 and target cells were reseeded at a density of 1,000,000 cells/2 ml/well in 6-well
1096 plates. On day 4 (48 h posttransfection), target cells were incubated with EnduRen
1097 live cell substrate (Promega, Cat# E6481) for 3 h and then detached, and 32,000
1098 target cells were applied to a 96-well plate with effector cells. RL activity was
1099 measured at the indicated time points using a Centro XS3 LB960 (Berthhold
1100 Technologies). The S proteins expressed on the surface of effector cells were
1101 stained with rabbit anti-SARS-CoV-2 S monoclonal antibody (GeneTex, Cat#
1102 GTX635654) and APC-conjugated goat anti-rabbit IgG polyclonal antibody (Jackson
1103 ImmunoResearch, Cat# 111-136-144). Normal rabbit IgG (SouthernBiotech, Cat#
1104 0111-01) was used as a negative control. Expression levels of surface S proteins
1105 were analyzed using a FACS Canto II (BD Biosciences). RL activity was normalized
1106 to the mean fluorescence intensity (MFI) of surface S proteins, and the normalized
1107 values are shown as fusion activity.
1108
1109 **Mathematical Modeling for Fusion Velocity Quantification**
1110 The following cubic polynomial regression model was employed to fit each of time-
1111 series datasets (**Figure 4E**):

1112
1113 $y \sim b_0 + b_1 x + b_2 x^2 + b_3 x^3$
1114
1115 The initial velocity of cell fusion was estimated from the derivative of the fitted cubic
1116 curve.
1117
1118 **Neutralization Assay**
1119 Virus neutralization assay was performed on HOS-ACE2/TMPRSS2 cells using the
1120 SARS-CoV-2 S pseudoviruses expressing luciferase (see "Pseudovirus Assay"
1121 above). The viral particles pseudotyped with D614G S or D614G/P681R S were
1122 incubated with serial dilution of heat-inactivated human serum samples or the RBD-
1123 targeting NAbs (clones 8A5, 4A3 and CB6; Elabscience) at 37°C for 1 h. The
1124 pseudoviruses without sera and NAbs were also included. Then, the 80 μl mixture
1125 of pseudovirus and sera/NAbs was added into HOS-ACE2/TMPRSS2 cells (10,000
1126 cells/50 μl) in a 96-well white plate and the luminescence was measured as
1127 described above (see "Pseudovirus Assay" above). 50% neutralization titer (NT_{50})
1128 was calculated using Prism 9 (GraphPad Software).
1129 For the cell-cell fusion neutralization assay, effector cells of the S-based
1130 fusion assay (i.e., S-expressing cells) were incubated with the serially diluted
1131 neutralizing antibodies targeting RBD (clones 8A5, 4A3 and CB6; Elabscience) at
1132 37°C for 1 h. Then, target cells were applied and performed the S-based fusion
1133 assay as described above (see "SARS-CoV-2 S-Based Fusion Assay" above).
1134
1135 **QUANTIFICATION AND STATISTICAL ANALYSIS**
1136 Data analyses were performed using Prism 9 (GraphPad Software). Data are
1137 presented as average with SD. In the figures except **Figure 5B**, n represents the
1138 number of technical replicate. In Figure 5B, n represents the number of serum donor.
1139 In **Figure 2A, 3B, 4B, 4D, 4E**, statistically significant differences were determined
1140 by Student's t test.
1141 In **Figures 2B and 2C**, statistically significant differences were determined by the
1142 Mann-Whitney U test.
1143 In **Figures 4F and 4G**, statistically significant differences were determined by were
1144 determined by two-sided Welch's *t* test.
1145 In **Figure 5B**, a statistically significant difference was determined by Wilcoxon
1146 matched-pairs signed rank test.